

# A new mathematical model for investigating solidification, solute transportation, and TiN precipitation in a micro-alloy steel containing Ti

Han Wang<sup>1</sup>, \*Tian-peng Qu<sup>1</sup>, Tian Liang<sup>2</sup>, \*\*Xiang-long Li<sup>1</sup>, De-yong Wang<sup>1</sup>, Lei Fan<sup>1</sup>, Zhi-xiao Zhang<sup>1</sup>, and Zheng-hong Yang<sup>3</sup>

1. School of Iron and Steel, Soochow University, Suzhou 215137, China

2. Institute of Metal Research, Chinese Academy of Sciences, Shenyang 110016, China

3. Jiangsu Jianai Shares High Temperature Material Limited Company, Wuxi 214200, Jiangsu, China

Copyright © 2025 Foundry Journal Agency

**Abstract:** In order to investigate the segregation process and clarify its effect on the formation of TiN during the solidification of a micro-alloy steel containing titanium (Ti), a new mathematical model concerning solute transportation, solidification, as well as TiN precipitation was successfully established and verified. The transportation of solute elements was described using the Brody-Fleming microsegregation model, while the thermodynamic principles governing the precipitation of TiN were derived within the framework of the model. Additionally, the model accounts for variations in the diffusion coefficient due to phase transition and the influence of non-equilibrium solidification on solute distribution. High-temperature tests were conducted to validate the mathematical model. Results show that during solidification, due to selective crystallization, there is positive segregation of Ti and N in the solidifying front. What's more, due to the high cooling rate near the surface of this steel, negative segregation is easier to be formed in the surface area. The highest concentration of TiN precipitation is found in the 1/4 width of this steel. High-temperature experiment shows that when the solidifying front reaches the 1/4 width of the specimen, the concentration product of Ti and N elements biased at the solidifying front reaches the thermodynamic conditions of TiN precipitation, and exists a higher concentration of TiN distributed in this region. To address this phenomenon, a comparative analysis of the effects of cooling rate and initial solute element content on TiN precipitation behavior was conducted. An increase in the surface cooling rate accelerates the progression of the solidification front and diminishes solute segregation near the front, thereby reducing TiN precipitation. However, with the increase of the initial solute element content, the concentration product of Ti and N elements rises, then the content of TiN precipitation increases. The results of this model provide important insight into the micro segregation and TiN precipitation mechanism of the micro-alloy steels bearing titanium.

**Keywords:** microsegregation; solute redistribution; precipitation of TiN; numerical simulation

CLC numbers: TG142.33

Document code: A

Article ID: 1672-6421(2025)03-333-12

## 1 Introduction

Micro-alloy steels containing Ti are characterized by excellent mechanical property and low cost, which are widely used in chemical equipment, aerospace plane,

ship building, as well as other fields [1-3]. During solidification and cooling process of this kind of steels, the precipitation of numerous inclusions such as TiC and TiN greatly damages the mechanical properties of final steel products [4-8]. The reason for this phenomenon is that the morphology of TiN is cubic or triangular, leading to stress concentration in the steels, especially at sharp corners, which result in crack defects [7, 8]. Consequently, gaining a thorough understanding of TiN precipitation is critical for mitigating its detrimental effects on steel, thereby enhancing both the performance and quality of the final rolled product.

### \*Tian-peng Qu

Professor. His research interests focus on solidification theory, continuous casting, and numerical simulation on industrial process.

E-mail: qutianpeng@suda.edu.cn

### \*\*Xiang-long Li

E-mail: xlli@suda.edu.cn

Received: 2024-08-14; Revised: 2024-09-23; Accepted: 2024-10-11

The mechanism of TiN precipitation, along with strategies for its control, has aroused wide concern in today's steel plants. Due to limitations in experimental technology, many researchers have turned to a combination of numerical simulation and experimental validation to explore the TiN precipitation process. Gui et al.<sup>[9]</sup> integrated a microsegregation model with a thermodynamic model of inclusion precipitation, comprehensively assessing the impact of TiN precipitation on steel quality. Their findings indicated that, irrespective of the macro-distribution of TiN in steels, a critical titanium content of 0.053wt.% achieved the highest toughness without being overly influenced by TiN inclusions. Liu et al.<sup>[10]</sup> conducted experiments to observe the morphology and distribution of TiN inclusions in cast billets, complementing their observations with thermodynamic modeling to determine the onset of TiN precipitation. They discovered that TiN particles began to precipitate when the solidification fraction exceeded 0.82, with 93% of the precipitation occurring by the end of solidification. This model was based on ideal thermodynamic equilibrium assumptions. Gui et al.<sup>[11]</sup> utilized the Vollere-Beckermann<sup>[12]</sup> microsegregation model to calculate elemental segregation, proposing the use of an equilibrium partition coefficient in the form of a phase-change and temperature-dependent function. This approach elucidated the precipitation mechanism of typical precipitation phases in high-sulfur steels, though it did not consider the effect of cooling rate on solute distribution. In reality, the cooling rate significantly influences both the timing and size of TiN precipitation<sup>[13-15]</sup>. However, the effect of cooling rate on solute distribution remains understudied. Thus, incorporating this factor could enhance the accuracy of the model. Furthermore, despite extensive research on microsegregation and inclusion precipitation in steel, the behavior of TiN precipitation under non-equilibrium thermodynamic conditions remains unclear. Thus, the main objective of this study is to develop a novel mathematical model that integrates solidification, segregation, and TiN precipitation, with the aim of elucidating the characteristics of TiN precipitation under various operational conditions.

Modeling of microsegregation is fundamental to the study of solute segregation<sup>[16-19]</sup>, with the solute equilibrium partition coefficient playing a crucial role in ensuring the accuracy of the mathematical models. In essence, the precision of the partition coefficient significantly influences large-scale segregation predictions<sup>[16, 17]</sup>. According to results achieved by Chen et al., the partition coefficients are heavily influenced by the composition of steels, solidification conditions, and phase transformation. Different solidification systems for liquid steel can result in varying partition coefficients<sup>[20]</sup>. These coefficients are typically determined through a combination of experimental measurements and theoretical calculations. Hobbs<sup>[21]</sup> used linear regression methods to calculate the solute equilibrium partition coefficients for nickel-based alloys based on experimental data, while Kagawa<sup>[22]</sup> analyzed the discrepancies between the equilibrium partition coefficients of binary iron-carbon alloys and ternary alloys during solidification

using theoretical approaches. However, achieving true theoretical equilibrium in practical scenarios is challenging<sup>[23]</sup>. Furthermore, variations in solute content that influence phase transformations at different proportions within the steel can markedly alter TiN precipitation<sup>[24]</sup>. Chen et al.<sup>[20]</sup> calculated the quantitative change of the partition coefficient considering the change of temperature and phase transformation during solidification of iron-carbon based hexahydroxy alloy. However, there is still a lack of the equilibrium partition coefficient research including solidification path and temperature research. Therefore, adjusting the solute equilibrium partition coefficient to make the model more closely align with actual conditions is the secondary objective of this study.

Moreover, numerous studies have highlighted the significant influence of inclusion distribution on quality of steels. Duan et al.<sup>[25]</sup> observed that the maximum number density of TiN occurs at the 1/4 thickness of a Ti-stabilized ultra-pure ferrite stainless steel. Similarly, Que et al.<sup>[26]</sup> investigated the distribution and growth behavior of TiN inclusions in a titanium-microalloyed steel. They found that when the solidification front moved to the center of the slab, the number density of TiN precipitates decreased while their average size increased, with the highest number density occurring at the 1/4 thickness. Liu et al.<sup>[27]</sup> demonstrated that precipitates and bubbles tended to accumulate at the 1/4 width of the slab, with a higher number density occurs near the inner arc side compared to the outer arc. Presslinger<sup>[28]</sup> noted that defects arising from precipitates and bubbles were challenging to eliminate through heat treatment processes and could substantially degrade steel properties. Consequently, elucidating the reasons for the formation of TiN precipitates in the radial 1/4 region of the slab's wide plane and developing strategies to control this phenomenon constitute the third objective of this study.

In summary, this study aims to integrate laboratory-scale high-temperature simulation experiments with numerical modeling to investigate the precipitation behavior of TiN through enhancements to the microsegregation model. The key innovations of this research include: (1) To deduce the principle of TiN precipitation so as to improve the accuracy of the micro-segregation mathematical model. (2) To design high-temperature experiments to reveal the concentration and distribution of TiN in the 1/4 width of a slab. (3) To reveal the effects of different operating conditions (cooling rate and initial Ti content) on the precipitation of TiN near 1/4 width of the steel slab. This study can provide theoretical guidance for the precipitation of TiN in titanium steel.

## 2 Mathematical model

### 2.1 Governing equations

The phenomena of solidification, solute transport, and chemical reactions in steel is governed by the mass, momentum, and energy equations. The model is applied comprehensively across the entire computational domain, encompassing the liquid, solid, and two-phase regions. These equations are detailed in Table 1.

Table 1: List of governing equations [29-32]

Equation	Expression	Nomenclature
Mass conservation equation	$\frac{\partial(\rho u_i)}{\partial x_i} = 0$	(1) $\rho$ Density ( $\text{kg}\cdot\text{m}^{-3}$ ) $u_i$ Velocity ( $\text{m}\cdot\text{s}^{-1}$ )
Momentum conservation equation	$\frac{\rho \partial(u_i u_j)}{\partial x_j} = -\frac{\partial P}{\partial x_i} + \frac{\partial}{\partial x_i} \left( \mu_{\text{eff}} \frac{\partial u_i}{\partial x_j} + \mu_{\text{eff}} \frac{\partial u_j}{\partial x_i} \right) + S$ $S = S_{i,\text{mom}} + S_{i,\text{p}}$ $S_{i,\text{p}} = \sum_i \rho g_i \beta_{c,i} (C_{1,i} - C_{0,i}) + \rho g_i \beta_T T - \rho g_i \beta_T T_1$ $S_{i,\text{mom}} = \frac{(1-f_1)^2}{f_1^3 + 0.001} A_{\text{mushy}} (u_i - v_p)$	(2) $\mu_{\text{eff}}$ Viscosity [ $\text{kg}\cdot(\text{m}\cdot\text{s})^{-1}$ ] $S$ Flow source term $S_{i,\text{mom}}$ Dynamic source term $S_{i,\text{p}}$ Buoyancy source term $P$ Pressure (Pa) (3) $\beta_T$ Thermal expansion coefficient ( $\text{K}^{-1}$ ) $\beta_{c,i}$ Solutal expansion coefficient ( $\text{wt}\cdot\%^{-1}$ ) $g_i$ Gravity ( $\text{m}\cdot\text{s}^{-2}$ ) (4) $T$ Temperature (K) $f_1$ Liquid phase mass fraction $v_p$ Casting speed ( $\text{m}\cdot\text{s}^{-1}$ ) (5) $A_{\text{mushy}}$ Mushy zone parameters $C_{1,i}$ Species concentration (wt.%) $C_{0,i}$ Initial concentration (wt.%)
Energy conservation equation	$\frac{\partial(\rho u_i H)}{\partial x_i} = \frac{\partial}{\partial x_i} \left( \lambda_{\text{eff}} \frac{\partial T}{\partial x_i} + \frac{C_p \mu_t}{Pr_t} \frac{\partial T}{\partial x_i} \right)$ $H = h + f_1 L$ $T_1 = T_{\text{pure}} - \sum_i G_i C_{1,i}$ $T_s = T_{\text{pure}} - \sum_i G_i C_{1,i} / k_i$	(6) $H$ Enthalpy ( $\text{J}\cdot\text{kg}^{-1}$ ) $\lambda_{\text{eff}}$ Thermal conductivity [ $\text{W}\cdot(\text{m}\cdot\text{K})^{-1}$ ] $C_p$ Specific heat [ $\text{J}\cdot(\text{kg}\cdot\text{K})^{-1}$ ] (7) $Pr_t$ Turbulent Prandtl number $h$ Sensible enthalpy ( $\text{J}\cdot\text{kg}^{-1}$ ) $L$ Latent heat ( $\text{J}\cdot\text{kg}^{-1}$ ) (8) $T_{\text{pure}}$ Melting point of pure iron (K) (9) $G_i$ Slope of the liquidus [ $\text{K}\cdot(\text{wt}\cdot\%)^{-1}$ ] $k_i$ Solute equilibrium partitioning coefficient
Species transport equation	$\frac{\partial(\rho u_i C_i)}{\partial x_i} = \frac{\partial}{\partial x_i} \left( \rho_{\text{eff}} \frac{\partial C_i}{\partial x_i} D_1^i + S_{\text{dif}} + S_{\text{con}} \right)$ $S_{\text{dif}} = \frac{\partial}{\partial x_i} \left( \rho f_s D_s^i \frac{\partial(C_{s,i} - C_i)}{\partial x_i} \right) + \frac{\partial}{\partial x_i} \left( \rho f_1 D_1^i \frac{\partial(C_{1,i} - C_i)}{\partial x_i} \right)$ $S_{\text{con}} = \frac{\partial}{\partial x_i} \left[ \rho (u_i - v_p) (C_{1,i} - C_i) \right]$ $C_i = f_s^i C_{s,i} + f_1^i C_{1,i}$	(10) (11) $D_1^i$ Solute diffusion coefficient ( $\text{m}^2\cdot\text{s}^{-1}$ ) $S_{\text{dif}}$ Diffusion source term $S_{\text{con}}$ Convection source term $f_s$ Solid fraction (12) $C_i$ Mixed concentration (wt.%) (13)
Microsegregation equation	$C_{1,i} = C_{0,i} \left( 1 + f_s (\beta_i k_i - 1) \right)^{\frac{1-k_i}{(\beta_i k_i - 1)}}$ $\beta_i = 2\alpha_i$ $\alpha_i = \frac{D_s^i t_f}{(\lambda/2)^2}$ $t_f = \frac{T_1 - T_s}{R}$ $\lambda = 125.85 R^{-0.4935}$	(14) (15) $\beta_i$ Back diffusion coefficient (16) $\alpha_i$ Fourier number $t_f$ Local solidification time (s) $R$ Cooling rate ( $\text{K}\cdot\text{s}^{-1}$ ) (17) $\lambda$ The secondary dendrite arm spacing $k_i^{\delta/1}$ Equilibrium partition coefficient in $\delta/1$ of solute $i$ (18) $k_i^{\gamma/1}$ Equilibrium partition coefficient in $\gamma/1$ of solute $i$ $k_i^{\delta+\gamma/1}$ Equilibrium partition coefficient in $\delta+\gamma/1$ of solute $i$
	$k_i = \begin{cases} k_i^{\delta/1} = \frac{C_i^\delta}{C_i^1} \\ k_i^{\gamma/1} = \frac{C_i^\gamma}{C_i^1} \\ k_i^{\delta+\gamma/1} = \omega_i^\delta \cdot k_i^{\delta/1} + \omega_i^\gamma \cdot k_i^{\gamma/1} \end{cases} \begin{cases} C_i^\delta = \frac{m_i^\delta}{m_\delta} \\ C_i^\gamma = \frac{m_i^\gamma}{m_\gamma} \\ C_i^1 = \frac{m_i^1}{m_1} \end{cases} \begin{cases} \omega_i^\delta = \frac{m_i^\delta}{m_i^\delta + m_i^\gamma} \\ \omega_i^\gamma = \frac{m_i^\gamma}{m_i^\delta + m_i^\gamma} \\ \omega_i^\delta + \omega_i^\gamma = 1 \end{cases} \quad (19)$	$C_i^\delta$ Concentration in $\delta$ (wt.%) $C_i^\gamma$ Concentration in $\gamma$ (wt.%) $C_i^1$ Concentration in liquid (wt.%) $\omega_i^\delta$ Mass percent in $\delta$ $\omega_i^\gamma$ Mass percent in $\gamma$

The initial components of steel is shown in Table 2. Figure 1 illustrates the equilibrium partition coefficients of the solute elements Ti and N in each phase. The Ti and N elements go through the  $L+\delta \rightarrow L+\delta+\gamma \rightarrow L+\gamma$  phase in turn, and the mass of the solute in each phase was calculated. Figures 1(a) and (c) represent the concentration of Ti and N in each phase, calculated by Eq. (19), Figs. 1(b) and (d) are the equilibrium partition coefficients of solute calculated from solute concentration. For element N, the equilibrium partition coefficient increases with decreasing temperature, which indicates that the segregation of solute element N decreases with decreasing temperature. For element Ti, the

equilibrium partition coefficient decreases with decreasing temperature, which indicates that the segregation of solute element Ti increases with decreasing temperature. Following the solidification process, the quantitative relationship equations for the equilibrium partition coefficients of Ti and N through regression analysis are as Eqs. (20-21):

$$k_{Ti} = \begin{cases} k_{Ti}^{\delta/1} = -4.29076 \times 10^{-6} T^2 + 0.01645 T - 15.38252 & 1746 < T \leq 1782 \\ k_{Ti}^{\delta+\gamma/1} = 0.0021 T^2 - 7.3579 T - 6437.02108 & 1737 \leq T \leq 1746 \\ k_{Ti}^{\gamma/1} = 2.48292 \times 10^{-5} T^2 - 0.08642 T + 75.40731 & 1721 < T \leq 1737 \end{cases} \quad (20)$$

$$k_N = \begin{cases} k_N^{\delta/1} = 3.64371 \times 10^{-6} T^2 - 0.013237 T + 12.30225 & 1746 < T \leq 1782 \\ k_N^{\delta+\gamma/1} = -0.00741 T^2 + 25.94281 T - 22696.69897 & 1737 \leq T \leq 1746 \\ k_N^{\gamma/1} = -1.09478 \times 10^{-4} T^2 + 0.38255 T - 333.69188 & 1721 < T \leq 1737 \end{cases} \quad (21)$$

Table 2: The initial concentration of each element in steel (wt.%)

Element	C	Si	Mn	P	S	Ti	N	Fe
Content	0.13	0.18	1.72	0.01	0.003	0.03	0.005	Bal.

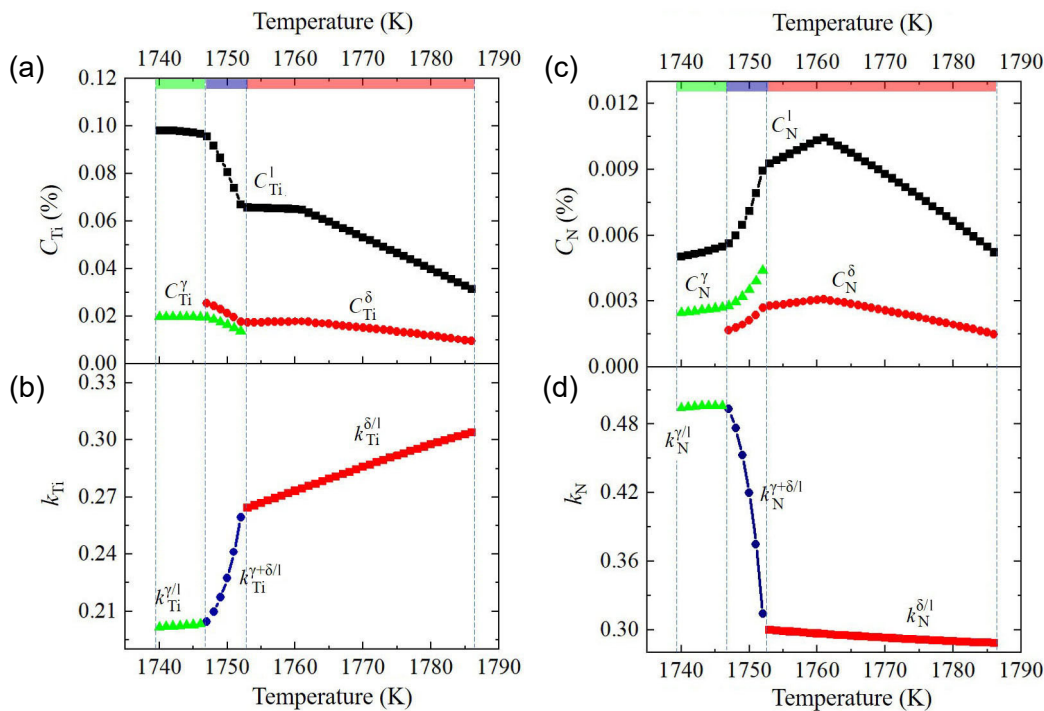
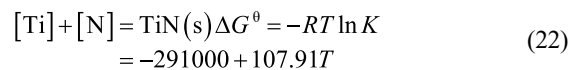


Fig. 1: Variation of solute equilibrium partition coefficient with temperature and phase constitution: (a) concentration of solute Ti in solid-liquid phase; (b) equilibrium partition coefficient of solute Ti; (c) concentration of solute N in solid-liquid phase; (d) equilibrium partition coefficient of solute N

## 2.2 Mechanism of TiN precipitation

Previous studies have reported that solute elements are typically pushed toward the liquid zone in steels, resulting in a notable increase in element concentration near the solidification front. The precipitation of TiN is known to depend on the equilibrium concentration product [33]. However, the underlying principle of TiN precipitation remains undetermined. Diverging from previous work, the principle of TiN reactions can be expressed by the following equation [34]:



$$K = \frac{\alpha_{TiN}}{\alpha_{[Ti]}\alpha_{[N]}} = \frac{1}{(f_{Ti} \cdot C_{Ti,eq}^f) \cdot (f_N \cdot C_{N,eq}^f)} \quad (23)$$

$$\lg K = -\frac{\Delta G^0}{2.3RT} = \frac{15220}{T} - 6.54 \quad (24)$$

$$\lg f_i = e_i^j [\%i] + e_i^j [\%j] + e_i^k [\%k] + \dots \quad (25)$$

where  $R$  is the thermodynamic constant,  $8.314 \text{ J} \cdot (\text{mol} \cdot \text{K})^{-1}$ ,  $T$  is the

temperature,  $K$ ,  $K$  is the equilibrium concentration product,  $\alpha$  is the activity of the phase, and TiN is a pure substance with an activity of 1;  $f$  is the activity coefficient;  $C_{Ti,eq}^f$  and  $C_{N,eq}^f$  are the equilibrium concentrations of solutes Ti and N in the liquid phase at the solid fraction  $f_s$ , respectively, and the solute interaction coefficients in the equations are shown in Table 3. Only when  $\Delta G < 0$ , the reaction goes to the right direction, which is then calculated as [33, 34],

$$\lg(C_{Ti,eq}^f \cdot C_{N,eq}^f) = 5.748 - \frac{14383}{T} \quad (26)$$

As stated above, TiN precipitates when the product of the solute concentrations ([Ti] and [N]) exceeds the equilibrium concentration product. Following this precipitation, the concentration product of the residual solute in the liquid phase equals to the equilibrium

concentration product. The quantity of TiN precipitation was calculated, as illustrated in Fig. 2. The  $C_{Ti,deplete}$  is the concentration of Ti depleted by the TiN formation reaction,  $C_{Ti,remnants}$  and  $C_{N,remnants}$  are the concentrations of Ti and N remnants produced by the TiN formation reaction,  $M_{Ti}$ ,  $M_N$ , and  $M_{TiN}$  are the relative molecular masses of solute Ti, N, and product TiN,  $C_{L,Ti}$  and  $C_{L,N}$  are the concentrations of solute Ti and N in the liquid phase before the TiN formation reaction, which are calculated by Eq. (14);  $C_{Ti,eq}^f \cdot C_{N,eq}^f$  is the equilibrium concentration product at the end of the TiN formation reaction, calculated by Eq. (26).

If  $C_{L,Ti} \cdot C_{L,N} < C_{Ti,eq}^f \cdot C_{N,eq}^f$ , there is no precipitation, then the concentration in the mesh will not change. If  $C_{L,Ti} \cdot C_{L,N} > C_{Ti,eq}^f \cdot C_{N,eq}^f$ , according to the principle of Fig. 2, the precipitation amount of TiN was obtained, the concentration of Ti and N in the mesh was corrected to the  $C_{Ti,remnants}$  and  $C_{N,remnants}$ , the segregation of solute and the precipitation of TiN in the next time were simulated, and so on until the end of

Table 3: Interaction coefficient of each element in molten steel [34]

Action coefficient	C	Si	Mn	P	S	Ti	N
$e_{Ti}$	-0.165	0.05	0.043	-0.064	-0.11	0.013	-1.8
$e_N$	0.13	0.047	-0.021	0.045	0.007	-0.53	0

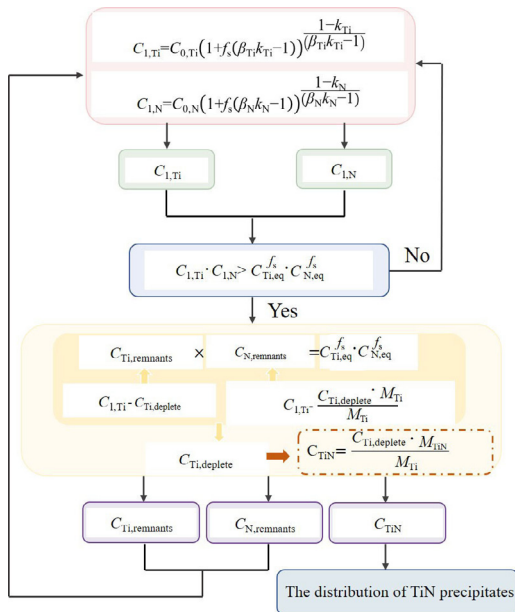


Fig. 2: Flow chart for the calculation of TiN precipitation amount

solidification. Specifically, the cooling rate [as defined in Eq. (17)] is calculated as the difference between the temperature at the previous time step and the current time step, divided by the length of the time step. This principle was implemented in Fluent through a user-defined function (UDF) to modify the segregation process.

### 2.3 Model setting

The physical model and the corresponding hexahedral mesh plot are depicted in Fig. 3. The minimum size of all meshes is 0.2 mm. The physical property parameters of the steel are shown in Table 4.

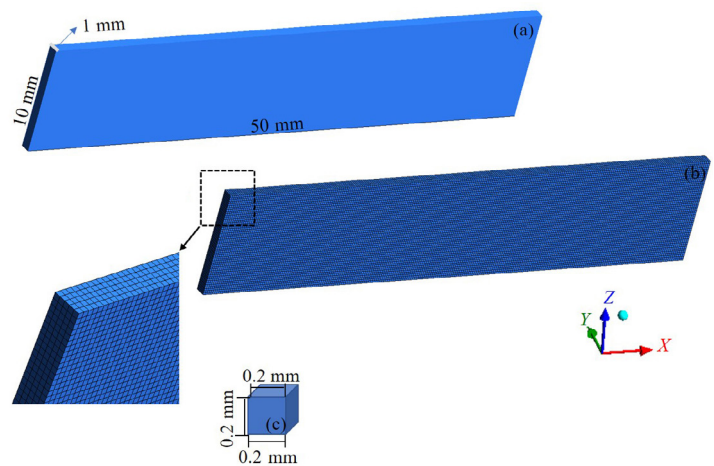


Fig. 3: Calculation model: (a) solidification calculation domain; (b) mesh division; (c) volume mesh

Table 4: Physical property parameters of steel

Physical property	Values
Density	7,330 kg·m <sup>-3</sup>
Specific heat	710 J·(kg·K) <sup>-1</sup>
Thermal coefficient	32 W·(m·K) <sup>-1</sup>
Viscosity	0.0051 kg·(m·s) <sup>-1</sup>
Latent heat	271,000 J·kg <sup>-1</sup>
Diffusion coefficients of Ti	$D_{\delta} 3.15 \exp(-247704.5/RT) \text{ cm}^2 \cdot \text{s}^{-1}$ $D_{\gamma} 0.15 \exp(-250968.2/RT) \text{ cm}^2 \cdot \text{s}^{-1}$
Diffusion coefficients of N	$D_{\delta} 0.008 \exp(-79081.3/RT) \text{ cm}^2 \cdot \text{s}^{-1}$ $D_{\gamma} 0.91 \exp(-168497.6/RT) \text{ cm}^2 \cdot \text{s}^{-1}$

### 3 Analysis of calculation results

#### 3.1 High-temperature experiment of TiN precipitation

To elucidate the distribution characteristics of TiN precipitates, predictions were validated through high-temperature experiments. A vacuum resistance furnace was used to melt 1,000 g of pure iron, and 500 ppm of titanium was added, N<sub>2</sub> was introduced at a flow rate of 0.72 L·min<sup>-1</sup> for 10 min. Finally, C block was added to adjust the composition of C in the steel. Through ICP analysis, the content of these three elements in the test sample is 0.15%C-0.035%Ti-0.0052%N. The mixture was then cooled to room temperature to produce a specimen with a width of 50 mm, as illustrated in Fig. 4. The thermocouple test shows that the average cooling rates are 0.065 °C·s<sup>-1</sup> in the middle of the molten pool and 1.15 °C·s<sup>-1</sup> in the surface layer. The specimen was longitudinally divided into three sections: No. 1, No. 2, and No. 3, as shown in Fig. 4. Following grinding and polishing, scanning electron microscopy was employed to scan 50 fields of view (each measuring 1 mm×0.17 mm) sequentially from No. 1 to No. 3. The observation position for the high-temperature test is located in the radial center area. In this region, solidification primarily occurs along the axial direction due to minimal radial heat transfer. Additionally, radial heat transfer at the top and bottom is negligible. The numerical simulation also focuses on axial heat transfer, assuming that there is no radial heat transfer in the region.

The scanning electron microscope and energy dispersive spectrometer analysis reveal the presence of TiN, with a relatively regular morphology as shown in Fig. 5. These TiN particles are mainly square or rectangular. Figure 6 illustrates the distribution of TiN along the radial centerline of the specimen's cross-section. It is observed that the TiN intensity is the lowest near the surface layer, with a trend of increasing firstly and then decreasing from the left side of the surface layer towards the center. Within the 1/4 width of the specimen, Point (a) exhibits the highest TiN concentration at 70.6 mm<sup>-2</sup>, whereas Point (c) in the surface layer shows a significantly lower number density at 11.7 mm<sup>-2</sup>, indicating minimal TiN distribution. The maximum number density of TiN in this region determined by the high temperature experiment is similar to the trend observed in the 1/4 width concentration distribution. In summary, this study presents microsegregation and TiN precipitation coupling numerical simulation results, which accurately predict the tendencies of TiN precipitation.

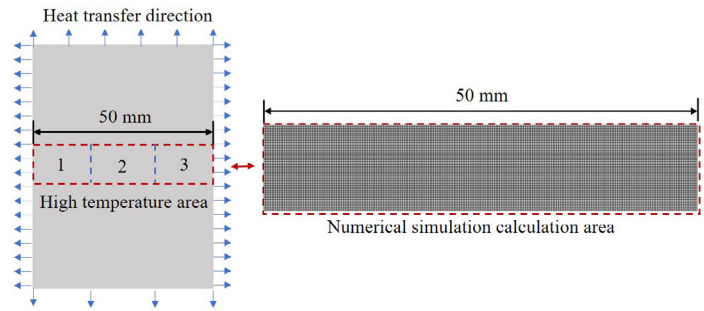


Fig. 4: High temperature test observation area and numerical simulation calculation model diagram

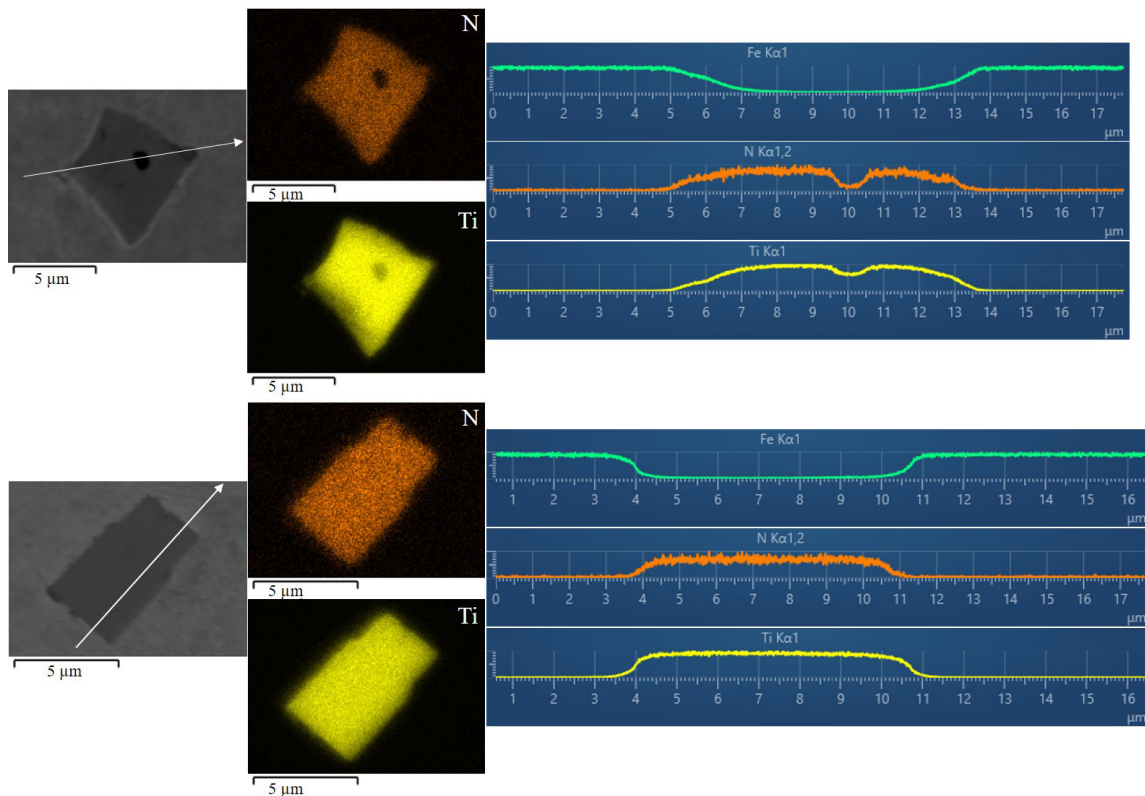


Fig. 5: Morphological characteristics of typical TiN

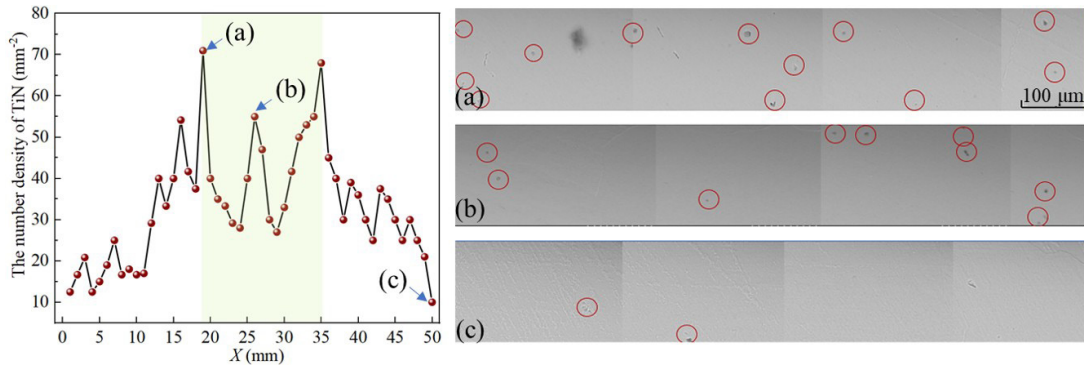


Fig. 6: Number density of TiN in the center of specimen and distribution of TiN under different fields of view

### 3.2 Solute elemental segregation behavior

Based on numerical simulation calculation, the contours of temperature at different times during the solidification process are shown in Fig. 7. At each moment, the temperature gradually increases from the surface layer to the center, while at the same position, it steadily decreases as solidification time increases. The contours of mass fractions of the solute elements Ti and N at various time points are illustrated in Fig. 8. Initially, these solute elements are uniformly distributed in the center plane, with the initial content being 0.03% for Ti and 0.005% for N. During solidification, concentration enrichment firstly occurs in the solid-liquid coexistence phases and then progresses

toward the center. By the end of solidification, the central concentration of Ti reaches 0.07%, exhibiting a maximum degree of segregation <sup>[33]</sup> of 2.3. Similarly, for N, the central concentration is 0.01%, with a maximum degree of segregation of 2. Both elements demonstrate positive segregation. As the solidification front moves from the surface to the center, the solute's solubility in the liquid phase consistently exceeds that in the solid phase. This results in spontaneous concentration enrichment toward the center, driven by chemical potential, leading to a higher concentration in the central region. Ti content at specific surface layer positions measures 0.007%, with a degree of segregation of 0.23, and N content measures 0.001%, with a degree of segregation of 0.2, indicating negative segregation phenomena. After the initial solidification, there is a significant difference in the solubility of the solute in the solid and liquid phase, and the solute always gathers in the liquid phase. Due to the advancement of the solute elements to the center, in the state of solute mass conservation, the surface layer will inevitably produce negative segregation.

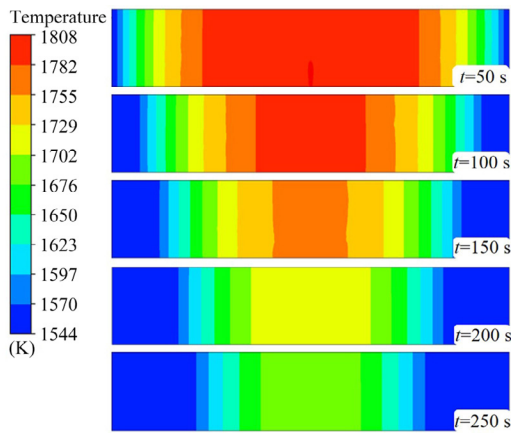


Fig. 7: Contours of temperature at different times

### 3.3 Characterization of TiN precipitation distribution

The initial heat transfer coefficient is  $1,000 \text{ W} \cdot (\text{m}^2 \cdot \text{K})^{-1}$ . Figure 9(a) illustrates the contours of the liquid fraction at various stages of solidification. As the solidification front advances toward the center, the solid phase forms. A two-phase coexistence region exists between the solid and liquid phases,

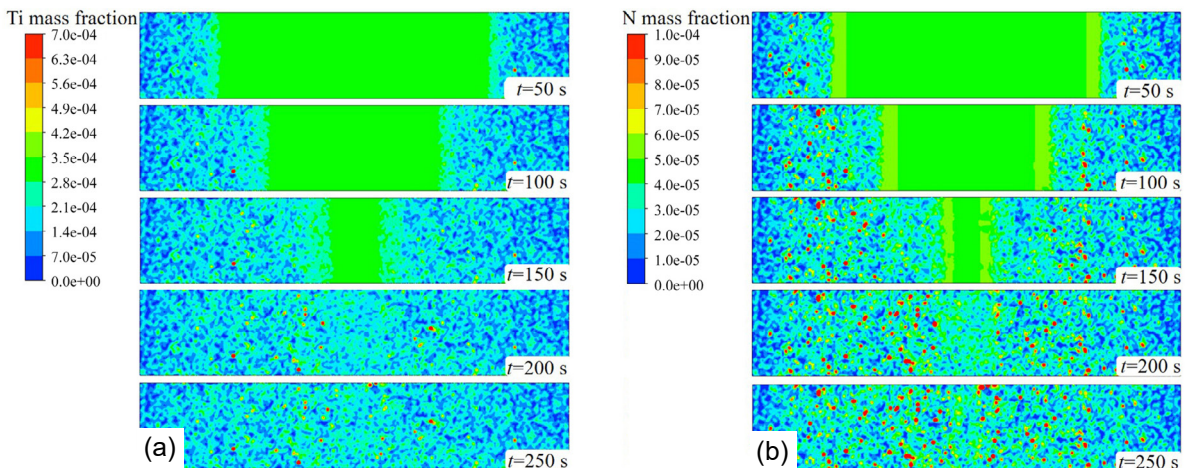


Fig. 8: Contours of mass fraction of solute elements at different times: (a) Ti; (b) N

with its width increasing as the solidification front moves inward. At the onset of solidification, the cooling rate is high, leading to a narrow secondary dendrite arm spacing and a correspondingly narrow two-phase coexistence zone. As the secondary dendrite arm spacing increases, the two-phase coexistence zone broadens. At a solidification time of 150 s, the solidification ratio (the ratio of the solidified area to the total area) is approximately 60%. By 250 s, the liquid phase has completely disappeared from the entire solidification area. Figure 9(b) depicts the TiN precipitation results at different solidification times. The surface layer shows less precipitation, and the amount of TiN precipitation varies at the same location over time. The TiN mass fraction increases progressively throughout the solidification process.

Upon solidification, the peak concentration of TiN precipitation is observed at one-quarter and three-quarters of the width, reaching an average concentration as high as 0.00034%. To determine this, a statistical analysis of the TiN concentration was conducted at each mesh point along the center plane. Then, the average concentration across the axial meshes was calculated and these values against radial distance were plotted, as illustrated in Fig. 10. Initially, the elements Ti and N are uniformly distributed,  $C_{1,Ti} \cdot C_{1,N} < C_{Ti,eq}^f \cdot C_{N,eq}^f$ , there is no TiN precipitation. While, as the elemental segregation

occurs, it results in a gradual enrichment of the solute concentration, and when  $C_{1,Ti} \cdot C_{1,N} > C_{Ti,eq}^f \cdot C_{N,eq}^f$ , the TiN starts to precipitate. The solidification front progresses to the radial 1/4 width point, where the solutes Ti and N are significantly concentrated, leading to a peak in TiN precipitation at this location. The variation in the amount of precipitation at the same point over different time periods is primarily influenced by the back diffusion coefficient in the microsegregation model. According to the Brody-Flemings microsegregation model, there is a finite diffusion within the solid phase. The accumulation of solutes is attributed to back diffusion, which prevents the achievement of the equilibrium concentrations,  $C_{Ti,eq}^f \cdot C_{N,eq}^f$  in the preceding computational step. Consequently, the solute concentrations are updated, creating conditions conducive to TiN precipitation.

### 3.4 Effect of cooling rate on TiN precipitation characteristics

The research model employs the heat transfer coefficient to characterize the heat transfer capacity between the fluid and the solid phase, with its numerical value reflecting the strength of the heat transfer. The heat transfer coefficient was set at four levels:  $1,500 \text{ W} \cdot (\text{m}^2 \cdot \text{K})^{-1}$ ,  $1,000 \text{ W} \cdot (\text{m}^2 \cdot \text{K})^{-1}$ ,  $500 \text{ W} \cdot (\text{m}^2 \cdot \text{K})^{-1}$ , and  $300 \text{ W} \cdot (\text{m}^2 \cdot \text{K})^{-1}$ . Figure 11 illustrates the contours of liquid

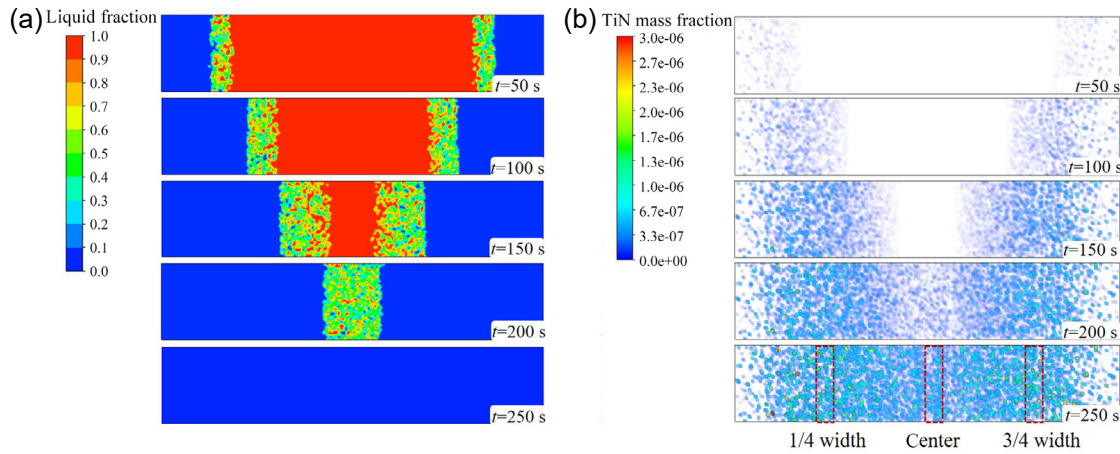


Fig. 9: Contours of liquid fraction at different times (a) and the contours of mass fraction of TiN at different times (b)

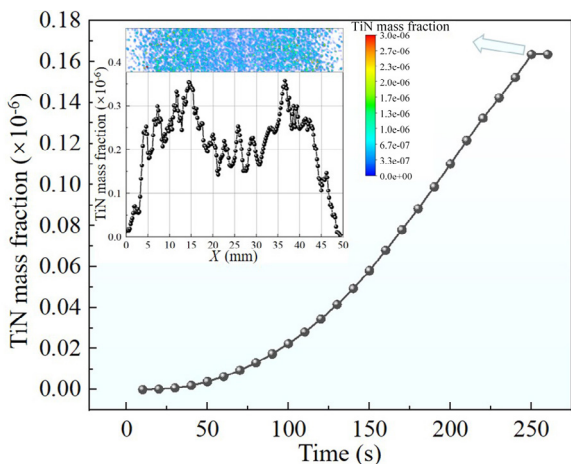


Fig. 10: Change of TiN mass fraction with time along radial direction on central plane at 250 s

fractions under identical solidification times but varying heat transfer conditions. For a solidification time of 100 s, the solidification rate is 25% at a heat transfer coefficient of  $1,000 \text{ W} \cdot (\text{m}^2 \cdot \text{K})^{-1}$  and 10% at  $500 \text{ W} \cdot (\text{m}^2 \cdot \text{K})^{-1}$ . This demonstrates that for the same solidification time, a higher convective heat transfer coefficient results in a faster cooling process.

The results of changes in liquid fraction and cooling rate under various heat transfer conditions and at solidification ratios of 25%, 40%, and 50% are shown in Fig. 12. Specifically, when the solidification ratio is 25%, the corresponding solidification times are 150 s, 90 s, 50 s, and 27 s under heat transfer conditions of 300, 500, 1,000, and  $1,500 \text{ W} \cdot (\text{m}^2 \cdot \text{K})^{-1}$ , respectively. The higher the heat transfer coefficient, the faster the cooling rate. For any given solidification ratio, a higher cooling rate narrows the two-phase coexistence zone during the solidification process.

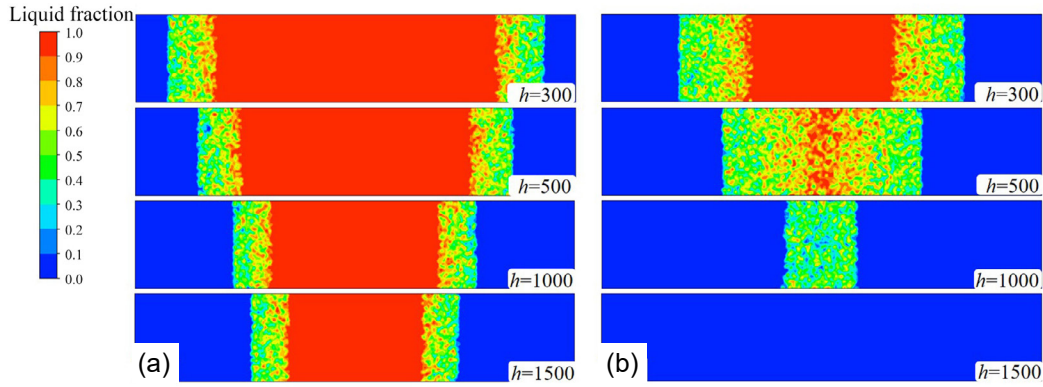


Fig. 11: Contours of liquid fraction under different heat transfer conditions but the identical solidification time: (a) 100 s; (b) 200 s

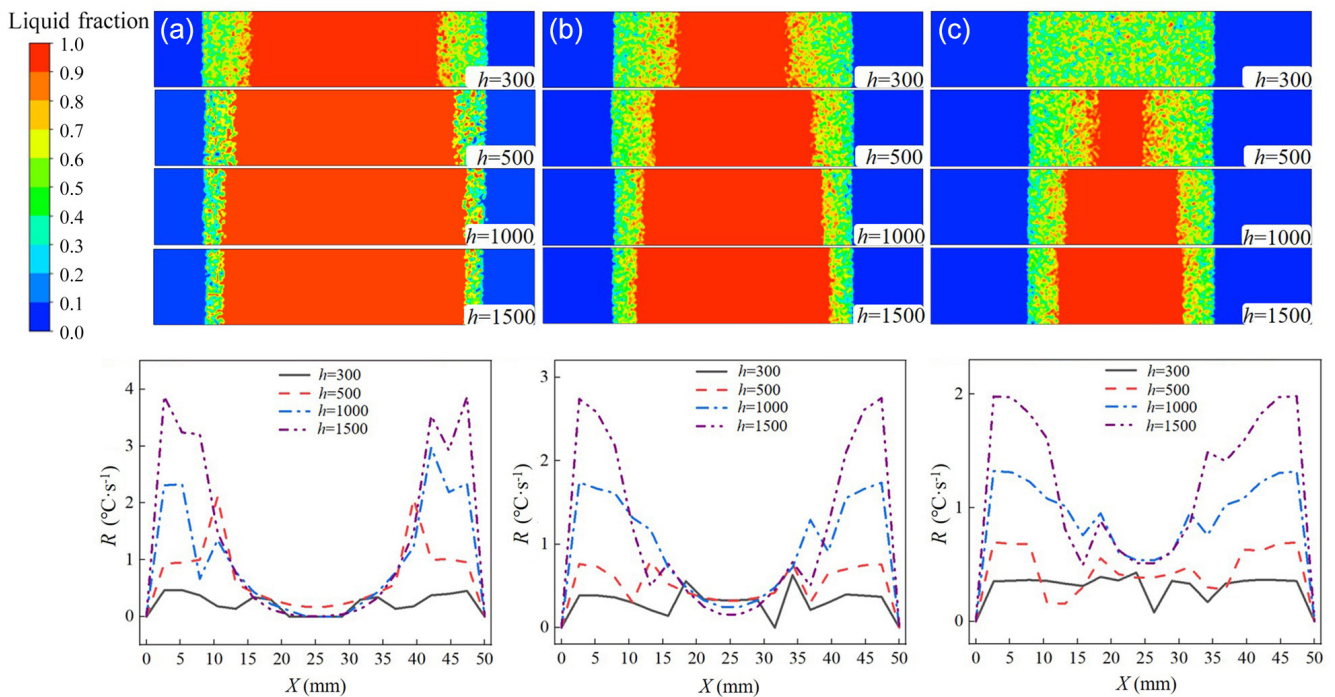


Fig. 12: Change of contours of liquid fraction and cooling rate at radial direction under different heat transfer conditions of 300, 500, 1,000, and 1,500  $W \cdot (m^2 \cdot K)^{-1}$  at different solidification ratios: (a) 25%; (b) 40%; (c) 50%

By calculating the precipitation behavior of TiN under three different solidification ratios, the average TiN concentration in the center plane along the radial direction was obtained, as shown in Fig. 13. Under the conditions of the same cooling rate but different solidification ratios, the concentration of precipitated TiN increases gradually with time. Notably, when considering the same solidification ratio but different cooling rates, the calculations reveal that the maximum value of the highest TiN concentration at a solidification ratio of 25% and various heat transfer coefficients of 300, 500, 1,000, and 1,500  $W \cdot (m^2 \cdot K)^{-1}$  is approximately 0.0002%, 0.00011%, 0.000046%, and 0.000024%, respectively. These findings indicate a gradual decrease in the highest concentration of TiN precipitation with increasing cooling rates.

The average concentration of TiN precipitates at the end of solidification under various cooling rates was calculated, as depicted in Fig. 14. The distribution of TiN precipitates

remains consistent across different heat transfer conditions, primarily concentrating in the 1/4 width region of the highest TiN concentration distribution. It has been confirmed that as the cooling rate increases, the average concentration of TiN precipitates steadily decreases. Cooling rate significantly influences solute segregation during the solidification process of steel. A higher cooling rate leads to a smaller secondary dendrite arm spacing, narrowing the two-phase coexistence zone where solute segregation occurs. This smaller spacing impedes solute segregation and reduces TiN precipitation. Additionally, at high solidification rates, there is less time available for solute diffusion. Although there is a thermodynamic drive for solute segregation, the kinetic drive is insufficient to support it within this brief timeframe. Consequently, element segregation at the solidification front weakens, leading to reduced TiN precipitation due to diminished solute segregation.

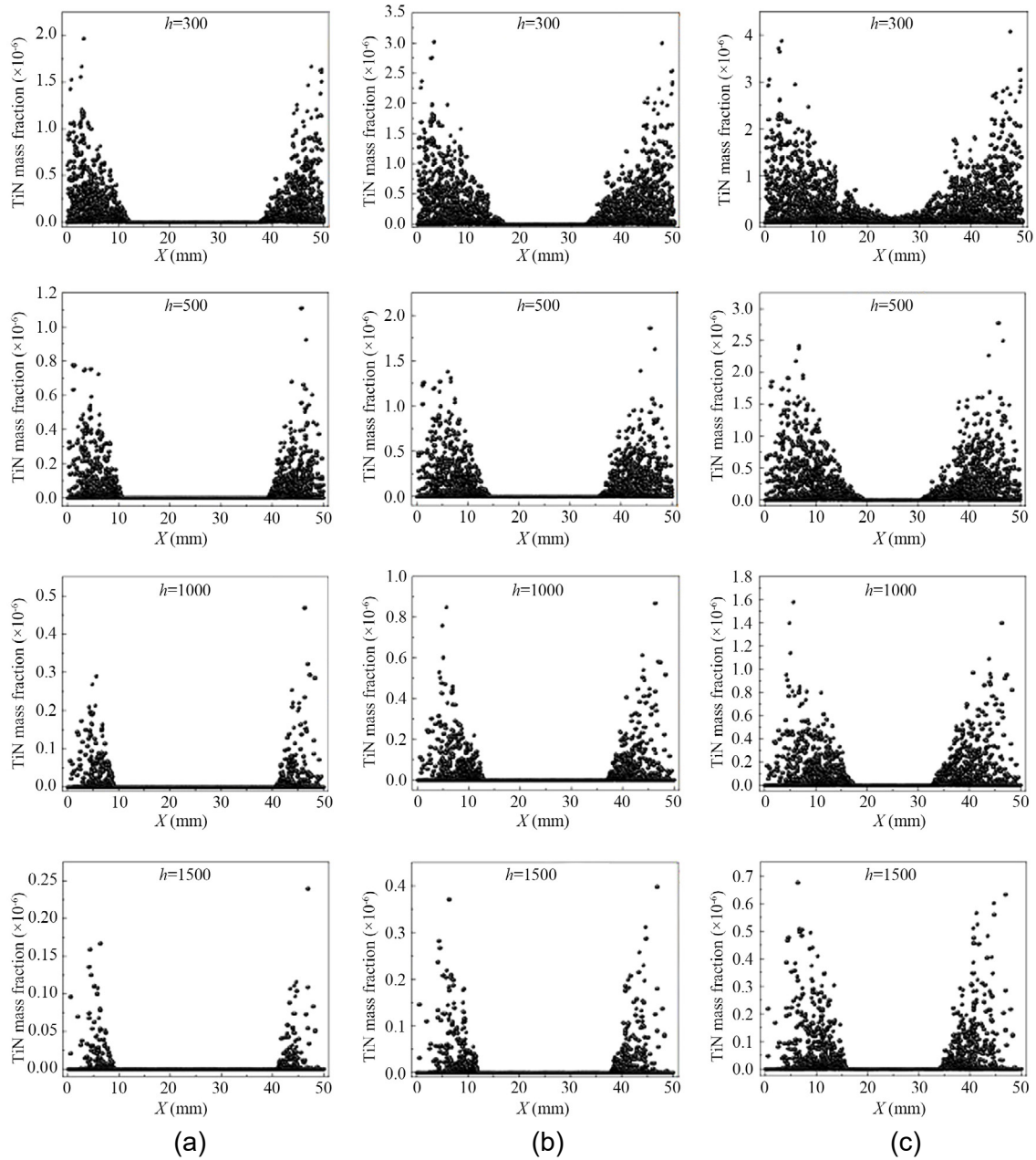


Fig. 13: Concentration distribution of TiN on the central plane under different heat transfer conditions of 300, 500, 1,000, and 1,500  $W \cdot (m^2 \cdot K)^{-1}$  at different solidification ratios: (a) 25%; (b) 40%; (c) 50%

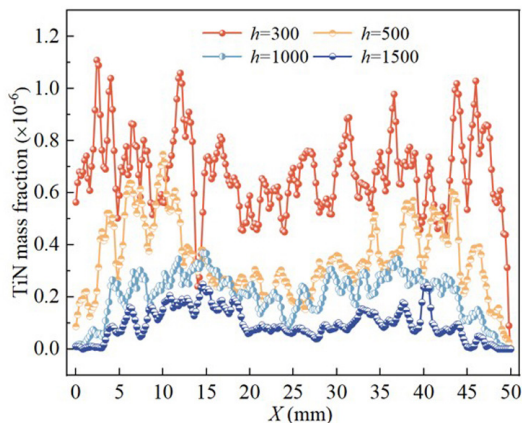


Fig. 14: Variation of TiN concentration with radial direction under different heat transfer conditions after solidification

### 3.5 Effect of initial Ti content on TiN precipitation characteristics

The variation of the average concentration of TiN precipitation with the radial direction and the contours of TiN mass fraction were analyzed, as depicted in Fig. 15. When the initial Ti content is 0.03%, the highest precipitation concentration of TiN can reach about 0.000035%. In comparison, when the initial Ti content is 0.02% and 0.04%, the maximum precipitation concentration of TiN is 0.000030% and 0.000041%, respectively. The cumulative amount of TiN precipitated over time for these initial Ti contents is illustrated in Fig. 16. Initially, no TiN precipitation occurs, however, as solidification progresses, the total amount of TiN precipitation steadily increases. At most of given points during solidification, the higher initial Ti content corresponds to the greater TiN

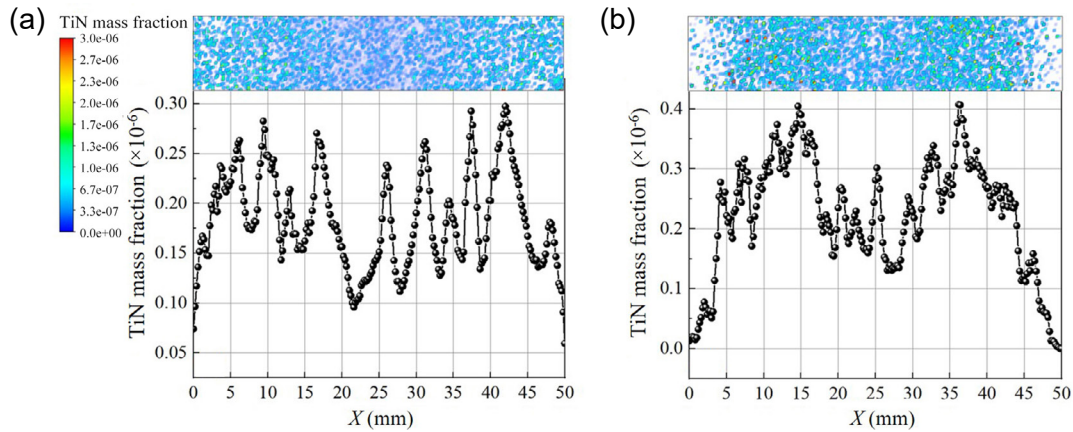


Fig. 15: Variation curves of TiN concentration on the central plane radial direction under different initial Ti content: (a) 0.02%; (b) 0.04%

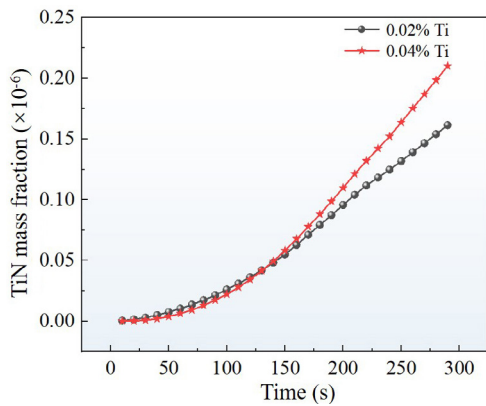


Fig. 16: Variation of mass fraction of TiN with time under different initial Ti content

precipitation. This phenomenon can be attributed to the increase in the amount of segregated solute element Ti as its initial content  $C_{0,i}$  [Eq. (14)] rises. This, in turn, leads to an increase in the concentration of TiN precipitation  $C_{TiN}$  [Eq. (14)]. Therefore, to control the precipitation of TiN and regulate the composition of steel inclusions, one can manage the initial solute content.

## 4 Conclusions

(1) To investigate the solidification process of micro-alloy steel bearing titanium, including solute element segregation and TiN precipitation laws, the numerical simulation methods were employed. Observations reveal that Ti and N solute elements migrate toward the center of the solidifying front, causing segregation. Specifically, the center position exhibits the highest degree of segregation, with Ti elements reaching a segregation degree of 2.23 and N elements achieving a segregation degree of 2. This leads to a pronounced positive segregation phenomenon. Conversely, at the surface where the cooling rate is high, the degree of segregation is significantly lower, with Ti elements showing a segregation degree of 0.23 and N elements displaying a segregation degree of 0.2, indicative of a negative segregation phenomenon.

(2) The concentration of TiN precipitation is the highest

at the 1/4 width. After the end of solidification, the average concentration of TiN precipitation is as high as 0.00005%. Furthermore, the highest concentration of TiN precipitation observed at the 1/4 width in the numerical simulation maintains the same trend as that observed in the high temperature experiment conducted at the same 1/4 width location.

(3) The precipitation of TiN is closely linked to the cooling rate and the initial solute content. A higher cooling rate tends to reduce TiN precipitation, whereas a higher initial solute content promotes its formation. Specifically, at a heat transfer coefficient of  $1,500 \text{ W} \cdot (\text{m}^2 \cdot \text{K})^{-1}$ , a faster cooling rate accelerates the solidification process and decreases the amount of TiN that precipitates. Compared to initial titanium content of 0.03% and 0.04%, a lower content of 0.02% yields a reduced concentration of TiN precipitation.

## Acknowledgments

This work was supported by the National Natural Science Foundation of China (Grant Nos. 52174321, 52274339, 52204348), the Jiangsu Achievement Transformation Fund Project (Grant No. SBA2023030047), and the Postgraduate Research & Practice Innovation Program of Jiangsu Province (Grant No. KYCX24\_3310).

## Conflict of interest

The authors declare that they have no competing financial interests or personal relationships that could have appeared to influence the work in this paper.

## References

- [1] Gao Z, Pan G, Song Y, et al. High cycle fatigue behavior of titanium microalloyed high-strength beam steels. *Journal of Iron and Steel Research International*, 2023, 30(11): 2267–2279.
- [2] Wang S, Gao Z, Wu G, et al. Titanium microalloying of steel: A review of its effects on processing, microstructure and mechanical properties. *International Journal of Minerals, Metallurgy and Materials*, 2022, 29(4): 645–661.

- [3] Meng C, Wang Y, Wei Y, et al. Strengthening mechanisms for Ti- and Nb-Ti-micro-alloyed high-strength steels. *Journal of Iron and Steel Research International*, 2016, 23(4): 350–356.
- [4] Tian Q, Wang G, Zhao Y, et al. Precipitation behaviors of TiN inclusion in GCr15 bearing steel billet. *Metallurgical and Materials Transactions: B*, 2018, 49(3): 1149–1164.
- [5] Ma W, Bao Y, Zhao L, et al. Control of the precipitation of TiN inclusions in gear steels. *International Journal of Minerals, Metallurgy, and Materials*, 2014, 21(3): 234–239.
- [6] Wang L, Xue Z L, Chen Y L, et al. Understanding TiN precipitation behavior during solidification of SWRH92A tire cord steel by selected thermodynamic models. *Processes*, 2019, 8(1): 10–23.
- [7] Wang Z, Xie J, Li Q, et al. TiN/ $\gamma$ -Fe interface orientation relationship and formation mechanism of TiN precipitates in Mn18Cr2 steel. *China Foundry*, 2021, 18(3): 180–184.
- [8] Wu H, Li X, Wang Z, et al. Effect of TiN on sulfide morphology of non-quenched and tempered steel. *Metals*, 2022, 12(9): 1402–1415.
- [9] Gui L, Long M, Zhang H, et al. Study on the precipitation and coarsening of TiN inclusions in Ti-microalloyed steel by a modified coupling model. *Journal of Materials Research and Technology*, 2020, 9(3): 5499–5514.
- [10] Liu X, Bao Y, Gu C, et al. Distribution and precipitation mechanism of TiN in industrial pure iron bloom. *Steel Research International*, 2023, 94(3): 481–491.
- [11] Gui L, Long M, Wu S, et al. Quantitative effects of phase transition on solute partition coefficient, inclusion precipitation, and microsegregation for high-sulfur steel solidification. *Journal of Materials Science & Technology*, 2019, 35(10): 2383–2395.
- [12] Voller V R, Beckermann C. Approximate models of microsegregation with coarsening. *Metallurgical and Materials Transactions*, 1999, 30(11): 3016–3019.
- [13] Wan Y, Gao S, Li M, et al. Enrichment characteristic of carbon atoms in solid-liquid zone of high carbon steel under different directional solidification rates. *China Foundry*, 2021, 18(5): 488–496.
- [14] Liang W, Wu R, Yuan Q, et al. Investigation on precipitation behavior and morphology of TiN particles in high-Ti low-carbon high-strength steel. *Transactions of the Indian Institute of Metals*, 2020, 73(1): 151–159.
- [15] Wang P, Li C, Wang L, et al. Thermodynamic analysis of TiN precipitation in SWRH92A high carbon tire cord steel under the influence of solute micro-segregations during solidification. *Metallurgical and Materials Transactions: B*, 2021, 52(4): 2056–2071.
- [16] Dong Q, Zhang J, Qian L, et al. Numerical modeling of macrosegregation in round billet with different microsegregation models. *ISIJ International*, 2017, 57(5): 814–823.
- [17] Shu Q, Visuri V V, Alatarvas T, et al. Model for inclusion precipitation kinetics during solidification of steel applications in MnS and TiN inclusions. *Metallurgical and Materials Transactions: B*, 2020, 51(6): 2905–2916.
- [18] Shu Q, Visuri V V, Alatarvas T, et al. A kinetic model for precipitation of TiN inclusions from both homogeneous and heterogeneous nucleation during solidification of steel. *Metallurgical and Materials Transactions: B*, 2022, 53(4): 2321–2333.
- [19] Clyne T W, Kurz W. Solute redistribution during solidification with rapid solid state diffusion. *Metallurgical Transactions: A*, 1981, 12(6): 965–971.
- [20] Chen H, Long M, Cao J, et al. Phase transition of peritectic steel Q345 and its effect on the equilibrium partition coefficients of solutes. *Metals*, 2017, 7(8): 288.
- [21] Hobbs R, Tin S, Rae C, et al. A castability model based on elemental solid-liquid partitioning in advanced nickel-base single-crystal superalloys. *Metallurgical and Materials Transactions: A*, 2005, 36(10): 2761–2773.
- [22] Kagawa K, Iwata K, Nofal A A, et al. Theoretical evaluation of equilibrium partition coefficients of solute elements in Fe-C-base quaternary and multicomponent systems. *Materials Science and Technology*, 1985, 1(9): 678–683.
- [23] Sung P, Poirier D. Liquid-solid partition ratios in nickel-base alloys. *Metallurgical and Materials Transactions: A*, 1999, 30(8): 2173–2181.
- [24] Luo L, Liu T, Li K, et al. Microstructures, micro-segregation and solidification path of directionally solidified Ti-45Al-5Nb alloy. *China Foundry*, 2016, 13(2): 107–113.
- [25] Duan H, Zhang Y, Ren Y, et al. Distribution of TiN inclusions in Ti-stabilized ultra-pure ferrite stainless steel slab. *Journal of Iron and Steel Research International*, 2019, 26(9): 962–972.
- [26] Que G, Song S, Nyembwe A, et al. TiN inclusions distribution in the composite cross section of titanium micro-alloyed steel slab: Thermo-chemical modeling and automatic statistic analysis. *Journal of Materials Research and Technology*, 2023, 26: 5383–5392.
- [27] Liu Z, Li B. Effect of vertical length on asymmetric flow and inclusion transport in vertical-bending continuous cast. *Powder Technology*, 2018, 323: 403–415.
- [28] Prelinger H, Mayr M, Kaltenbrunner T, et al. Quantitative assessment of segregates in continuously cast slabs by electron probe microanalysis. *Steel Research*, 2002, 73(4): 149–156.
- [29] Ren N, Li J, Panwisawas C, et al. Thermal-solutal-fluid flow of channel segregation during directional solidification of single-crystal nickel-based superalloys. *Acta Materialia*, 2021, 206: 116620.
- [30] Ren N, Panwisawas C, Li J, et al. Solute enrichment induced dendritic fragmentation in directional solidification of nickel-based superalloys. *Acta Materialia*, 2021, 215: 117043.
- [31] Brody H D. Solute redistribution in dendritic solidification. *Massachusetts Institute of Technology*, 1965, 236(5): 615.
- [32] Won Y M, Thomas B G. Simple model of microsegregation during solidification of steels. *Metallurgical and Materials Transactions: A*, 2001, 32(7): 1755–1767.
- [33] Shang T, Wang W, Kang J, et al. Precipitation behavior of TiN in solidification of 20CrMnTi under continuous casting conditions. *Journal of Materials Research and Technology*, 2023, 24: 3608–3627.
- [34] Jin Y L, Du S L. Precipitation behaviour and control of TiN inclusions in rail steels. *Ironmaking & Steelmaking*, 2018, 45(3): 224–229.
- [35] Yang Q S, Duan J X, Deng A Y, et al. Numerical simulation of macrosegregation phenomenon in Cu-6wt%Ag alloy ingots fabricated by electromagnetic stirring. *Journal of Materials Research and Technology*, 2024, 28: 300–315.